

1 **Earth's radiation belts ions: patterns of the spatial-energy structure**
2 **and its solar-cyclic variations**

3 **Alexander S. Kovtyukh**

4 Skobeltsyn Institute of Nuclear Physics, Moscow State University, Moscow, 119234, Russia;
5 kovtyukhas@mail.ru

6 **Abstract** Spatial-energy distributions of the stationary fluxes of protons, helium and ions of
7 carbon-nitrogen-oxygen (CNO) group, with energy from $E \sim 100$ keV to 200 MeV, in the
8 Earth's radiation belts (ERB), at $L \sim 1-8$, are considered here using data from satellites in the
9 period 1961–2017. It has been found that the results of these measurements line up in the space
10 $\{E, L\}$ following some regular patterns. The ion ERB shows a single intensity peak that moves
11 toward Earth with increasing energy and decreasing ion mass. Solar-cyclic (11-year) variations
12 in the distributions of protons, helium and CNO group ions fluxes in the ERB are studied. It has
13 been observed that in the inner regions of the ERB, fluxes decrease with increasing solar
14 activity and that the solar-cyclic variations of fluxes of $Z \geq 2$ ions are much greater than for
15 protons; moreover, it seems that they increase with increasing atomic number Z . It is suggested
16 that heavier ion intensities peak further from the Earth and vary more over the solar cycle
17 because they have more strong ionization losses. These results indicate also that with variations
18 in the level of solar activity the coefficient D_{LL} of the radial diffusion of the ERB ions change
19 much less than the ionization loss rates of ions with $Z \geq 2$.

20
21
22 **Keywords.** Magnetospheric physics (energetic particles, trapped). Radiation belts.
23

24 1 Introduction

25 The ERB consist mainly of charged particles with energy from $E \sim 100$ keV to several hundreds of
26 megaelectronvolt (MeV). These particles are trapped by the geomagnetic field at altitudes from \sim
27 200 kilometers to ~ 50 – 70 thousands kilometers. The ERB consists mainly of electrons and
28 protons, but there are also helium nuclei and other $Z > 2$ ions (like oxygen etc), where Z is the
29 charge of the atomic nucleus with respect to the charge of the proton. During geomagnetic
30 disturbances, ion fluxes, and their distributions are changed. These fluxes depend also on the phase
31 of the solar cycle, conditions in the interplanetary space, and other factors.

32 Particles with different energy E and pitch angles α (α is the angle between the local vector of
33 the magnetic field and the vector of a particle velocity), which are injected into some point of the
34 geomagnetic trap, drift conserving the adiabatic invariants (μ , K , Φ) around the Earth (Alfvén
35 and Fälthammar, 1963; Northrop, 1963). Therefore, experimental data on the ERB are often
36 represented in coordinates $\{L, B\}$, where L is the drift shell parameter and B is the local induction
37 of the magnetic field (McIlwain, 1961). For the dipole magnetic field, L is a distance, in the
38 equatorial plane, from the given magnetic field line to the center of the dipole itself (in Earth's radii
39 R_E).

40 The stationary fluxes J of the ERB particles with given energy and pitch angle α decrease
41 usually when the point of observation is shifted from the equatorial plane to higher latitudes along
42 a certain magnetic field line (if we exclude the peripheral regions of the geomagnetic trap, where
43 the drift shells of the captured particles are split and branched). This dependence is described by
44 the functions $J(B/B_0)$, where B and B_0 are values of the magnetic field at the point of observation
45 and in the equatorial plane on the same magnetic field line, respectively.

46 Outer and inner regions of the ERB are maintained in dynamic equilibrium with the
47 environment by different mechanisms (see review Kovtyukh, 2018).

48 The outer belt ($L > 3.5$) is formed mainly by the mechanisms of radial diffusion of ions towards
49 the Earth under the action of fluctuations of both electric and magnetic fields resonating with their
50 drift periods (see, e.g., Schulz and Lanzerotti 1974; Kovtyukh, 2016b). This transport is
51 accompanied by the betatron acceleration and by the ionization losses of the ions as a result of
52 their interactions with the plasmasphere and with residual atmosphere.

53 The inner belt ($L < 2.5$) of protons with $E > 10$ MeV is formed mainly as a result of decay of
54 neutrons knocked from the nuclei of the atmospheric atoms by the Galactic Cosmic Rays (GCR)-
55 $\text{F}\ddot{\text{O}}\text{r}$; for protons with $E < 10$ MeV this mechanism (CRAND) is supplemented by the radial
56 diffusion of particles from the outer to the inner belt (see, e.g., Selesnick et al., 2013, 2014). The
57 inner belt of ions with $Z > 4$ is formed mainly from the ions of the Anomalous component of
58 Cosmic Rays (see, e.g., Mazur et al., 2000).

59 In the intermediate region ($2.5 < L < 3.5$), the mechanism of a ion capture from Solar Cosmic
60 Rays takes place during strong magnetic storms (see, e.g., Selesnick et al., 2014).

61 Thus, the main mechanisms of formation of the ERB, together with the sources of injection and
62 losses of ions, are known. However, for a comprehensive verification of the physical models and to
63 identify the mathematical models and their parameters, the formulation of complete and reliable
64 empirical representations of the ERB for each of the ion components, is necessary; it is also
65 necessary for ensuring the safety of space flights.

66 These models can be created only using experimental data, obtained over many years and
67 decades; such models (see, e.g., Ginet et al., 2013) were already created for protons (AP8/AP9)
68 and they are widely used in space research. On the contrary, measurements of $Z \geq 2$ ion fluxes
69 suffer from technical problems due to small statistics and high background of protons and
70 electrons. For this reasons, empirical and semi-empirical models for $Z \geq 2$ ions, are applicable
71 only to very limited regions of the space $\{E, L\}$.

72 One of the main problems of this work is to consider the possibility to create sufficiently
73 complete and reliable empirical models of the ERB for these ions based on currently available
74 experimental data.

75 In the following sections, the spatial-energy structure of the ERB in the $\{E, L\}$ space for
76 protons, helium and CNO group ions are considered (Sect. 2) together with possible physical
77 mechanisms of formation of these structures and their solar-cyclic variations (Sect. 3). Finally, the
78 main conclusions of this work are given (Sect. 4).

79 **2 Spatial-energy distributions of the ion fluxes near the equatorial plane**

80 There can be ions trapped in drift shells only with energies less than some maximum values,
81 determined by the Alfvén's criterion: $\rho_i(L, E, M_i, Q_i) \ll R_c(L)$, where ρ_i is the gyroradius of ions,
82 and R_c is the radius of curvature of the magnetic field near the equatorial plane (M_i and Q_i are mass
83 and charge of ions with respect to the corresponding values for protons). According to this
84 criterion and to the theory of stochastic motion of particles, the geomagnetic trap in the dipolar
85 region can capture and durably hold only ions with E (MeV) $< 2000 \times (Q_i^2/M_i) L^{-4}$ (Ilyin et al.,
86 1984). The green line in Figs 1-6 represents this very boundary.

87 When comparing the data of various experiments in the ERB, the question arises about the
88 compatibility of these results with each other and the reasons for their discrepancies. A significant
89 number of these discrepancies can be connected to the differences in their trajectories; in the
90 construction of the instruments and their angular characteristics; in the energy ranges and sets of
91 energy channels. For the stationary ERB, these discrepancies can also be associated with
92 differences in the general state of the Sun, heliosphere and magnetosphere of the Earth during
93 various periods of data-taking. These factors influence the fluxes of ions with $Z \geq 2$ in the ERB
94 more significantly with respect to proton fluxes (see, e.g., Kovtyukh, 2018).

95 In this section, experimental data of various satellites, which were obtained for quiet periods
96 ($Kp < 2$) and near the equatorial plane of the ERB for ions with equatorial pitch angles $\alpha_0 \approx 90^\circ$
97 have been used. In the regions of E and L shells, where these data were obtained, the ion fluxes are
98 not distorted by the background of other particles.

99 In many important experiments, the instruments were not able to separate fluxes of ions by their
100 charge. Moreover, for the ions of the CNO group, the separation by mass are not usually
101 performed. For heavier species, for example for Fe ions, we have very small data-sets. Therefore,
102 this work presents data on helium ions (without any charge separating) and CNO ions (without any
103 mass or charge separation).

104 To solve the aforementioned problems, it is important to choose the form of representation
105 (space of variables), in which the results of every experiment can be compared to the others. In our
106 case, the space $\{E, L\}$ has been used; this choice is very efficient to better organize fragmentary
107 experimental data obtained in different ranges of E and L .

108 Figures 1–6 show the spatial-energy distributions of the fluxes of protons, helium ions, and ions
109 of the CNO group near the equatorial plane. Odd figures refer to periods near the minima, and
110 even figures refer to periods near the solar activity maxima. The values E and L in these figures are
111 presented in logarithmic scales. Statistical and methodical errors of the experimental points on
112 these figures do not exceed of the size of these points. The markers are connected by lines of equal
113 intensity of ion fluxes (iso-lines); the decimal logarithms of the fluxes J , in unit of $(\text{cm}^2 \text{ s ster}$
114 $\text{MeV/n})^{-1}$, are shown near each iso-lines.

115 Such representations of the experimental data are not only visual, but also very convenient and
116 rather universal. Obviously, Figs. 1–6 actually show both radial profiles of the fluxes of ions for a
117 given energy and ion energy spectra for a given L shell.

118 The points in Figs. 1–6 have been obtained from the radial profiles of fluxes $J(L)$ for the
119 average energies of the ions in the channels of the instruments. Unlike electron fluxes or ion fluxes

120 measured during geo-active conditions, the ion fluxes considered here (i.e. during quiet periods),
121 have only one maximum in the functions $J(L)$. As a result, for each energy channel of the
122 respective mission, 1 or 2 points were obtained (on the outer and inner edges of these profiles) with
123 certain values of E and L for a given level of ion fluxes. Sometimes, especially for fluxes, only one
124 point was obtained: in these cases, the radial profile of the ion fluxes was cutoff at small values of
125 L due to a significant background of contaminating particles and no interpolation/extrapolation has
126 been performed whatsoever.

127 Each iso-line, shown in these figures, has been evaluated separately from the corresponding set
128 of experimental points (icons); then it was transferred (along with the icons) to the corresponding
129 figure; thus, in more abundantly populated sectors of the plots (i.e. for protons with $E > 1$ MeV at
130 $L > 2$) such iso-lines are mixing in Figs. 1–2. In case of a large distance between neighboring
131 points, the corresponding segments of the iso-lines are shown as dashed arcs.

132 The radial profiles of the differential fluxes $J(L)$ of particles with different energy tend to
133 intersect with each other in those regions where the energy spectra present some local maximum or
134 minimum. On the contrary, the iso-lines cannot intersect with each other: because this would mean
135 that, at the same point in the space $\{E, L\}$, the ion fluxes differ very significantly (by an order of
136 magnitude) for quiet periods. Such uncertainty does not have a physical sense and a special
137 analysis is needed to identify other possible sources of errors.

138 Representing plots in a different space of variables would lead to more significant
139 methodological errors and uncertainties, because of the natural differences in the instrumentation
140 of the experiments taken into account; thus, a series of approximations or
141 interpolation/extrapolation techniques would become inevitable.

142 2.1 Spatial-energy structure of the proton fluxes

143 There is a large number of experimental data concerning ERB protons; the most important of them
144 are presented in Figs. 1 and 2. These figures serve as a comparison with similar distributions of $Z \geq$
145 2 ions (Figs. 3–6).

146 Figure 1 sums up results from the satellites Relay-1 (Freden et al., 1965); Ohzora or EXIS C:
147 Exospheric Satellite C, Akebono or EXOS-D: Exospheric Satellite D and ETS-VI: Engineering Test
148 Satellite (Goka et al., 1999). These results have been collected during minimum periods of various
149 solar cycles, i.e. between 19th / 20th (1963), 21th / 22th (1984–1985), and 22th / 23th (1994–1996) of
150 the solar activity cycles.

151 Figure 2 sums up results from the satellites 1968-81A (Stevens et al., 1970), Injun-5 or
152 Explorer-40 (Krimigis, 1970; Venkatesan and Krimigis, 1971; Pizzella and Randall, 1971), 1969-
153 025C or OV1-19: Orbiting Vehicle 1-19 (Croley et al., 1976), Azur or GRS A: German Research
154 Satellite A (Hovestadt et al., 1972; Westphalen and Spjeldvik, 1982), Molniya-1 (Panasyuk and
155 Sosnovets, 1973), GEOS-2: Geodetic Earth Orbiting Satellite 2 (Wilken et al., 1986), CRRES: The
156 Combined Release and Radiation Effects Satellite (Albert et al., 1998; Vacaresse et al., 1999), GEO-
157 3: Geostationary Orbit 3 (Selesnick et al., 2010) and Van Allen Probes (Selesnick et al., 2014,
158 2018). These results were obtained during maximum periods of 20th (1968–1971), 22th (1990–
159 1991), 23th (2000), and 24th (2012–2017) solar cycles.

160 The data of the satellites Explorer-45 (Fritz and Spjeldvik, 1979, 1981) and ISEE-1:
161 International Sun-Earth Explorer 1 or Explorer-56 (Williams, 1981; Williams and Frank, 1984) are
162 given in both Figs. 1 and 2 because solar-cyclic variations of the ERB proton fluxes are negligible
163 at $L > 2.5$ (see, e.g., Vacaresse et al., 1999).

164 From a comparison of Figs. 1 and 2, one can see that at $L < 2.5$ (especially at $L < 1.4$) the proton
165 fluxes during solar minima (Fig. 1) are higher than during maxima (Fig. 2). In addition, in the
166 former the inner edge of the proton belt is less steep and it can reach smaller L shells (for $E > 1$
167 MeV). The distributions of protons in the space $\{\mu, L\}$ (see, e.g., Kovtyukh, (2016a,b) , which I
168 have been constructed from Figs. 1 and 2 confirm these conclusions.

169 In Figs. 1 and 2, the iso-lines of proton fluxes are almost parallel to each other on $L > 3$ at
 170 sufficiently high energies. Since these iso-lines have separated from each other by approximately
 171 equal intervals on a logarithmic scale of the energy, this region in the space $\{E, L\}$ corresponds to
 172 power-law spectra of the ERB protons: for power-law spectra, $J \propto E^{-\gamma}$, where the index $\gamma =$
 173 $-\Delta(\log J)/\Delta(\log E)$. In these figures, this region is located between the green and red lines.

174 The red line corresponds to the lower boundary (E_b) of the power-law tail of the proton spectra.
 175 For this line, $E_b \sim 36 \times L^{-3}$ MeV. Some changes in the slope of these iso-lines at $L > 6$ can be
 176 connected to a discrepancy between the real configuration of the magnetic field lines and the
 177 dipolar configuration (used here for L shells calculation and for the red line).

178 For the dipole magnetic field region, the points on the red line correspond to particles with a
 179 specific value of the 1st adiabatic invariant of motion (μ_b). For Figs. 1 and 2, the average value μ_b
 180 is ~ 1.16 keV nT⁻¹. Segments of an iso-lines, that are parallel to the red line, also correspond to
 181 certain values of the invariant μ . In this region of the space $\{E, L\}$ the ionization and other losses
 182 of the ERB protons during radial drift can be neglected, and changes of fluxes with changing L are
 183 practically reduced to adiabatic transformations in a magnetic field.

184 It results from these figures that at $L = 3-6$, the value $\gamma = 4.8 \pm 0.5$. At $L > 6$ the distances
 185 between these iso-lines increase with L , and the value γ is decreased from $\sim 4.7-5.0$ at $L = 6$ to \sim
 186 $4.1-4.5$ at $L = 8$. This is due to the deviation of the magnetic field from the dipole configuration as
 187 well as to the increasing variability of this field with increasing L .

188 According to the data of satellites considered in (Kovtyukh, 2001), invariant parameters μ_b and γ
 189 were found only at $L > 3$. In this work, a wider range of L and E is considered, and for protons with
 190 $E > 10$ MeV these parameters can be traced to $L \sim 2$. At $L = 2$, $\gamma = 4.4 \pm 0.6$ (Fig. 1) and $\gamma = 4.7 \pm 1.3$
 191 (Fig. 2). This is due to the fact that the energy range is significantly extended toward higher values
 192 (up to 200 MeV), but here the ionization losses for protons rapidly decrease (see, e.g., Schulz and
 193 Lanzerotti, 1974; Kovtyukh, 2016a).

194 2.2 Spatial-energy structure of the helium ion fluxes

195 In Figs. 3 and 4 helium ion fluxes, averaged for quiet periods ($Kp < 2$), are presented.

196 Figure 3 sums up results from the satellites Molnija-2 (Panasyuk et al., 1977), Prognoz-5
 197 (Lutsenko and Nikolaeva, 1978), ISEE-1: The International Sun-Earth Explorer 1 (Hovestadt et al.,
 198 1981); Akebono or EXOS-D: Exospheric Satellite D and ETS-VI: Engineering Test Satellite (Goka et
 199 al., 1999). These results have been collected during minimum periods of various solar cycles, i.e.
 200 between 20th / 21th (1975–1977), 21th / 22th (1984–1985), and 22th / 23th (1994–1996) of the solar
 201 activity cycles.

202 Figure 4 sums up results from the satellites OV1-19: Orbiting Vehicle 1-19 (Blake et al., 1973;
 203 Fennell and Blake, 1976), Explorer-45 (Fritz and Spjeldvik, 1978, 1979; Spjeldvik and Fritz,
 204 1981), SCATHA: Spacecraft Charging At High Altitudes (Blake and Fennell, 1981; Chenette et al.,
 205 1984). These results were obtained during maximum periods of 20th (1968–1971) and 21th (1979)
 206 solar cycles.

207 From a comparison of Figs. 1–2 with Figs. 3–4, one can see that at $L > 2$ for helium ions the
 208 solar-cyclic (11-year) variations are greater than for protons. For example, at $L \sim 2-3$ from
 209 maximum to minimum of solar activity fluxes of protons with $E > 1$ MeV practically do not
 210 change, and the fluxes of helium ions with $E > 1$ MeV/n are increased by one order of magnitude.

211 Figures 3 and 4 show the same patterns as for protons, but the distribution of helium ion fluxes
 212 is slightly shifted towards higher values of L shell (with respect to protons). Unlike protons, there
 213 are significant “white spots” in these figures: because there are no experimental data for helium
 214 ions in these regions.

215 The red line on these figures corresponds to the lower boundary of the power-law tail of the
 216 helium ions spectra. For this line, $E_b/M_i \sim 43.4 \times L^{-3}$ MeV/n (Fig. 3) and $E_b/M_i \sim 21.7 \times L^{-3}$ MeV/n

217 (Fig. 4). If one takes into account that at $L < 6$ for helium ions with $E > 0.2$ MeV/n the average
 218 charge $Q_i = +2$ (see, e.g. Spjeldvik, 1979), then for the considered boundary we get: $\mu_b \sim 1.4 \times Q_i$
 219 keV/n \times nT $^{-1}$ at the maximum of solar activity and $\mu_b \sim 1.4 \times M_i$ keV/n \times nT $^{-1}$ at the minimum of solar
 220 activity (for the dipole magnetic field region). The iso-lines of helium ion fluxes in Figs. 3 and 4,
 221 which pass above the red line at $L > 2.5$, correspond to an average value of $\gamma \sim 5.5$ (there is a large
 222 uncertainty due to the small covered energy range).

223 For helium spectra, as for protons ones, the values of the parameters of the power-law tail are in
 224 agreement with what has been found in (Kovtyukh, 2001).

225 At the same time, one can see that the iso-lines of the fluxes of helium ions in the region above
 226 the red line (i.e. in the region of power-law spectra) substantially deviate from the slope of the red
 227 line. At $L > 3$ the fluxes of helium ions with given energy are increase with decreasing L slower
 228 than it is for protons. This means that the ionization losses of the ERB helium ions significantly
 229 exceed these losses for protons, in agreement to well-known calculations (see, e.g., Schulz and
 230 Lanzerotti, 1974). For example, Coulomb loss rate increases with increasing Z of the ions as Z^2 .

231 **2.3 Spatial-energy structure of the CNO group ions fluxes**

232 In Figs. 5 and 6 CNO group ions fluxes, averaged for quiet periods ($K_p < 2$), are presented.

233 Figure 5 sums up results from the satellites ATS-6: Applications Technology Satellite 6
 234 (Spjeldvik and Fritz, 1978; Fritz and Spjeldvik, 1981) and ISEE-1: The International Sun-Earth
 235 Explorer 1 (Hovestadt et al., 1978). These results have been collected during minimum period
 236 between 20th / 21th of the solar activity cycles (1974–1975, 1977).

237 Figure 6 sums up results from the satellite Explorer-45 (Spjeldvik and Fritz, 1978; Fritz and
 238 Spjeldvik, 1981). These results were obtained during maximum period of activity in 20th solar
 239 cycle (1971–1972).

240 On Figs. 5–6 the spatial-energy patterns of the ion fluxes of the CNO group are even more
 241 shifted towards higher values of L shell and its configuration differ significantly from Figs. 1–4.

242 From a comparison of Figs. 1–2 with Figs. 5–6 one can see that, for ions of CNO group, the
 243 solar-cyclic (11-year) variations are greater than for protons. For example, at $L \sim 3$ –5 from
 244 maximum to minimum of solar activity fluxes of protons with $E > 1$ MeV practically do not
 245 changed, but the fluxes of the CNO group increase by one order of magnitude or more. From a
 246 comparison of Figs. 3–4 with Figs. 5–6 it is seen also that the fluxes of CNO group change several
 247 times more than the fluxes of helium ions do.

248 This means that, for ions of the CNO group, the ionization losses at $L = 3$ –5 are much larger
 249 than for ions with $Z \leq 2$ and these losses have a significant effect even on the power-law segment
 250 of the spectra of the CNO ions (in the part which is seen on Figs. 5–6). Therefore, the lower
 251 boundary of the power-law tail of these ions spectra have not been obtained by the experiments
 252 collected in Figs. 5 and 6. The red line on these figures corresponds to adiabatic laws (see
 253 Kovtyukh, 2001); this line let us estimate the deviations from these laws. As can be seen from Fig.
 254 5–6, ionization losses for ions of the CNO group are especially large at the peak of solar activity
 255 (Fig. 6): during these times, the slope of iso-lines on $L > 3$ is significantly less than the slope of the
 256 red line.

257 At the same time, at $L > 4$ in Fig. 5 and at $L > 3$ in Fig. 6, the iso-lines of fluxes pass almost
 258 parallel to each other and at approximately equal distances from each other; the average value of γ
 259 corresponding to them is ~ 6 (there is a large uncertainty due to the small covered energy range).
 260 Thus, for sufficiently large values of E and L , the CNO group ions spectra in the ERB have a
 261 power-law form, but these spectra are softer in comparison with the spectra of protons.

262 The red line corresponds here to the dependences $E_b/M_i \approx 43.4 \times L^{-3}$ MeV/n (on Fig. 5) and E_b/M_i
 263 $\sim 12.4 \times L^{-3}$ MeV/n (on Fig. 6), which are taken from (Kovtyukh, 2001) where this boundary was
 264 more clearly defined also for the ions of the CNO group. If one takes into account that at $L \sim 3$ –5

265 for the CNO group ions with $E > 0.1$ MeV/n the average charge $Q_i = +4$ (see, e.g., Spjeldvik and
 266 Fritz, 1978), then for this boundary one can get: $\mu_b \sim 1.4 \times Q_i$ keV/n \times nT $^{-1}$ at the maximum of solar
 267 activity and $\mu_b \sim 1.4 \times M_i$ keV/n \times nT $^{-1}$ at the minimum of solar activity (for the dipole magnetic field
 268 region).

269 3 Discussion

270 Let us consider the conclusions following the results obtained here for solar-cyclic variations in the
 271 fluxes of ERB ions. Solar-cyclic (11-year) variations of proton fluxes with $E > 1$ MeV in the inner
 272 region of the ERB have been studied in many works (see, e.g., Pizzella et al., 1962; Hess, 1962;
 273 Blanchard and Hess, 1964; Filz, 1967; Nakano and Heckman, 1968; Vernov, 1969; Dragt, 1971;
 274 Huston et al., 1996; Vacaresse et al., 1999; Kuznetsov et al., 2010; Qin et al., 2014). These
 275 variations reach one order of magnitude at $L = 1.14$ and are reduced rapidly with increasing L (see,
 276 e.g., Vacaresse et al., 1999). However, solar-cyclic variations of fluxes of ions with $Z \geq 2$ have not
 277 been considered in these works.

278 In these works, such variations of the proton fluxes of the inner belt are connected to the solar-
 279 cyclic variations of the energy loss rates of protons in this region. For protons with $E > 10$ MeV of
 280 the inner ERB, the effect of attenuation of GCR proton fluxes in the Earth's orbit with increasing
 281 solar activity acts in the same direction (see, e.g., Usoskin et al., 2005; Selesnick et al., 2007). We
 282 must also take into account a secular variations of the geomagnetic dipole moment (see, e.g.,
 283 Selesnick et al., 2007).

284 Consider in more detail the solar-cyclic variations of the ERB ions fluxes in connect to
 285 variations of the energy loss rates of these ions. In quiet periods, only the mechanism of ionization
 286 loss is significant for the ERB protons trapped in small L shells (see, e.g., Schulz and Lanzerotti,
 287 1974). Energy loss rates and lifetimes of the ERB protons are determined, in this mechanism, by
 288 the density of atmospheric atoms and ionospheric plasma (N) in a geomagnetic trap. This density
 289 depends on the intensity of the ultraviolet radiation of the Sun. With decreasing solar activity (with
 290 a transition from maximum to minimum of the solar cycle), the densities of atmospheric atoms and
 291 ionospheric plasma in a geomagnetic trap are decreased and the stationary proton fluxes will
 292 increase with decreasing solar activity.

293 The lifetimes of protons increase with L ; this leads to a decrease in the amplitude of the solar-
 294 cyclic variations of proton fluxes. A proton lifetime on a given L shell depends on its energy and is
 295 less than 11 years ($\sim 3.5 \times 10^8$ s) at $L < L_c(E)$. For example, for protons with $E > 6$ MeV the value L_c
 296 is ~ 2.5 and corresponds to protons with $\mu > 3$ keV nT $^{-1}$ (see, e.g., Kovtyukh, 2016b, Fig. 3). Figs.
 297 1 and 2 show that for protons the solar-cyclic variations of fluxes are small and localized at $L < 2.5$
 298 (mainly at $L < 1.4$).

299 In contrast to protons, Figs. 3–6 show significant solar-cyclic variations of fluxes of helium ions
 300 and CNO group ions at $L \sim 2$ –5. There is low density of atmospheric atoms and ionospheric
 301 plasma in that region (compared to $L < 2$), but the density is changes consistently with solar
 302 cycle.

303 For ions with $Z \geq 2$ in the ERB, ionization losses are more significant than for protons and this
 304 can be connected to the absence of ions with $Z \geq 2$ at $L < 2$ (or very low values of these fluxes)
 305 during quiet geomagnetic conditions. Such short lifetimes are manifested also in the slope of the
 306 experimental curves in Fig. 4 and 6 (this was noted in sections 2.2 and 2.3, respectively).
 307 Consequently, for ions with $Z \geq 2$, the regions in which variations can manifested, should be
 308 located on higher L shells (at the same energies as for protons).

309 The lifetimes of ions in the energy ranges considered here are $\tau \propto M_i^{-1/2} Q_i^{-2} N^{-1} E^{3/2}$ (Schulz and
 310 Lanzerotti, 1974). In a first approximation, for $N \propto L^{-4}$, we obtain the value $L_{ci} \sim M_i^{1/8} Q_i^{1/2} L_c$, where
 311 L_c corresponds to the L shell of protons of the same energy of the other ions under study. For helium
 312 ions ($M_i = 4$, $Q_i = 2$) with $E \sim 6$ MeV, we obtain outer boundary $L_{ci} \sim 4.2$. For ions of CNO group (M_i

313 = 14, $Q_i = 4$) with $E \sim 6$ MeV we obtain outer boundary $L_{ci} \sim 6.9$. These are very rough estimations,
314 but they are in agreement with the results presented in Figs. 3–6.

315 These estimates are based on the following assumption: during variations in solar activity, the rates
316 of ion supply on $L < L_{ci}$ remains unchanged (or these changes are weaker than the effect of changes of
317 the rate of ion losses). The stationary ion fluxes of the ERB at $L > 2.5$ form mainly under the action of
318 radial diffusion (see, e.g., Schulz and Lanzerotti, 1974; Kovtyukh, 2016b, 2018). Therefore, the solar-
319 cyclic variations of $Z \geq 2$ ion fluxes can be motivated only under the assumption that the effect
320 related with an increase in the ionization losses of such ions significantly exceeds the effect
321 connected with the possible enhance of radial diffusion of ions during the rising phase of solar
322 activity. For example, when compare the empirical model of the inner belt ($L < 2.4$) of protons with E
323 ~ 19 – 200 MeV, constructed on the data of Van Allen Probes satellites, with the mathematical model
324 of radial diffusion of protons in this region, it was assumed that on the phase of growth of solar
325 activity from 2013 to 2015, D_{LL} increases by ~ 2 times (Selesnick and Albert, 2019).

326 In the experimental results presented here for the ERB ions, the region of the power-law tail of
327 the ion spectra is distinguished. For many experiments, especially for heavy ions, the values of the
328 parameter of a power-law tail spectra are determined much more accurately by the dependences
329 $J(L)$ of the ion fluxes (in logarithmic scale) for different pairs of energy channels (see Kovtyukh,
330 2001). For example, the range of L , in which these dependences for two energy channels are
331 parallel to each other is connected to the power-law tail of the spectra. Instead, on smaller values
332 of L , these fluxes begin to converge and the radial dependences of these fluxes intersect with each
333 other, which is related to the maximum in the spectra.

334 The main source of ions in the outer regions of the ERB is the solar wind, and usually the high-
335 energy part of these spectra have an exponential shape (see, e.g., Ipavich et al., 1981a, 1981b).
336 Immediately before being captured into the magnetosphere, these ions pass through a highly
337 turbulized regions, but the high-energy part of their spectra usually retains an exponential shape.
338 Therefore, the question arises: what physical mechanism converts the form of ion spectra from
339 exponential to power-law?

340 Evidently, the power-law tail of the ERB ions spectra must be generated-in the outer regions of
341 the magnetosphere. The most likely region for this to happen is the plasma sheet (PS) of the
342 magnetospheric tail, which is adjacent to the geomagnetic trap. The high-energy part of the ion
343 spectra in the PS, at $R \sim 20$ – $40 R_E$, has a power-law shape and the exponents of these spectra are
344 close to the corresponding parameters of the spectra of ions in the ERB. On the data of the
345 satellites IMP-7 and IMP-8 (Sarris et al., 1981; Lui et al., 1981) and also satellite ISEE-1 (Christon
346 et al., 1991), the shape of the ion spectra of the PS usually do not change during substorms; they
347 produce only parallel shifts of the spectra along logarithmic axes E and J . These results point out
348 that the time scales of formation processes of these ion spectra in the PS exceed the times of
349 substorms.

350 Parameters of the power-law tail of the ion spectra of the outer belt (γ and μ_b) reflect,
351 apparently, the most fundamental features of the mechanisms of acceleration of ions in the tail of
352 the magnetosphere. One can try to connect the values of these parameters with the most general
353 representations of the mechanisms of ion acceleration in the PS of the magnetospheric tail.

354 Most likely, this part of the ion energy spectra is formed in the PS by stochastic mechanisms of
355 ion acceleration; this hypothesis is supported by many experimental results. The statistical aspect
356 of these mechanisms reveals itself, in particular, in the fact that the ratios of fluxes (and partial
357 densities) of ions with different Z can differ, even greatly, at low and high energies. During their
358 wander in the phase space, ions gradually loose information about their origin and, therefore, the
359 high-energy tails of their spectra contain ambiguous information on the partial densities of
360 different components of ions in the source (see, e.g., Kovtyukh, 2001).

361 The high-energy part of the ion spectra of the PS can be generated by the mechanisms of
362 acceleration of particles on magnetic irregularities moving with respect to each other (Fermi

363 mechanism). The fractal structures of the PS are revealed on scales from ~ 0.4 to ~ 8 thousands
364 kilometers, for example, in the data of the satellite Geotail (Milovanov et al., 1996).

365 Under equilibrium conditions, this parameter is determined by the average part of energetic ions
366 in the total energy density of particles and magnetic irregularities ($\bar{\beta}$). From the theory which was
367 developed by Ginzburg and Syrovatskii (1964), it follows: $\gamma - 1 \approx (1 - \bar{\beta})^{-1}$. With increasing $\bar{\beta}$ in
368 the interval $0 < \bar{\beta} < 1$, the value γ increases monotonically and $\gamma \rightarrow \infty$ for $\bar{\beta} \rightarrow 1$. For real
369 average values $\bar{\beta}$ in the central PS $\bar{\beta} = 0.6\text{--}0.7$ (see, e.g., Baumjohann, 1993, Fig. 1), we get $\gamma =$
370 $3.5\text{--}4.3$.

371 Spectra with power-law tail and quasi-exponential segment at lower energies can be generated
372 when the value $\Delta B / \bar{B}$ for magnetic irregularities is proportional to their size δr and their spectral
373 density decreases rapidly with increasing δr for $\delta r < r_s$ (r_s is a thickness of the central PS), but for
374 $\delta r > r_s$ it remains almost unchanged. Apparently, the spectra of magnetic irregularities in the PS
375 have just such form (see, e.g., Milovanov et al., 1996). Then, the lower boundary μ_b of the power-
376 law tail corresponds to the condition $r_s / \rho_i \sim 10$, where ρ_i is the gyroradius of ions (see, e.g., Alfvén
377 and Fälthammar, 1963), i.e. $\mu_b \sim 0.02(Q_i^2 / M_i) B_s r_s^2$ keV nT $^{-1}$, where B_s is the average magnetic
378 field induction in the PS (in nT) and r_s is normalized to the Earth's radius. Using $B_s \sim 30$ nT and r_s
379 $\sim 1.3 R_E$ (see, e.g., Baumjohann, 1993) it can be obtained: $\mu_b \sim 1.0 (Q_i^2 / M_i)$ keV nT $^{-1}$. This value is
380 similar to the lower boundary of the power law spectrum which we find for the ERB protons,
381 suggesting that not only the slope of the spectrum but also its validity range can be explained with
382 scattering at magnetic irregularities.

383 The energy spectra of ions in the radiation belts of such planets as Jupiter and Saturn have the
384 form analogous to that of ion spectra in the ERB (see, e.g., Krimigis et al., 1981; Cheng et al.,
385 1985; Kollmann et al., 2011). As that in the ERB, these spectra have a long power-law tail, which
386 is formed, apparently, by mechanisms of stochastic acceleration of ions as a result of their
387 interactions with the current layer of the magnetospheric tail.

388 4 Conclusions

389 In this work, the experimental results for the stationary fluxes of the main ion components of the
390 ERB (protons, helium ions and ions of the CNO group) in the near equatorially plane, have been
391 analyzed. It has been found that in the outer belt these fluxes line up in the certain regular
392 patterns in the space $\{E, L\}$. The degree of similarity increases with increasing E and L and it is
393 linked to the nature of the main sources and on the universality mechanisms of transfer,
394 acceleration and losses of ERB ions in the outer belt (radial diffusion which conserves μ and K of
395 ions, betatron acceleration and ionization losses).

396 Moreover, solar-cyclic (11-year) variations of the spatial-energy distributions of the ERB ion
397 fluxes have been investigated. It has been noted that the ERB ions fluxes are weaker with
398 increasing solar activity and this effect increases with increasing atomic number Z . This kind of
399 dependence of the amplitude of flux changes on Z is typical, also, for faster variations in the fluxes
400 of the ERB ions, during geomagnetic storms and other disturbances of the Earth's magnetosphere,
401 as has been underlined in the review Kovtyukh (2018).

402 The figures presented here make it possible to determine in which regions of the space $\{E, L\}$
403 near the equatorial plane the ionization losses of ions during their radial diffusion can be neglected
404 and where this cannot. These results indicate also that with variations in the level of solar activity
405 the coefficient D_{LL} of the radial diffusion of the ERB ions change much less than the ionization
406 losses rates of ions with $Z \geq 2$.

407 In addition, the figures given here reveal the localization of “white spots”, especially extensive for
408 ions with $Z \geq 2$ and $E > 1$ MeV/n at $L < 3$. As Z and energy become larger and L becomes smaller,
409 the uncertainties in the values of the ERB fluxes become larger. These gaps must be filled by the

410 results of future experiments on satellites; for now, the extensive gaps in $Z \geq 2$ ion data do not allow
411 to create sufficiently complete and reliable empirical models of the ERB for these ions.

412

413 **Acknowledgements.** The author would like to thank the reviewers, Anonymous Referee #1
414 and Peter Kollmann (Applied Physics Laboratory, Johns Hopkins University), for very important
415 and fruitful comments and proposals to the paper.

416 **Financial support.** This work was supported by Russian Foundation for Basic Research RFFI
417 grant No. 17-29-01022.

418 References

- 419 Alfvén, H., and Fälthammar, C.-G.: *Cosmical Electrodynamics, Fundamental Principles*,
420 Clarendon Press, Oxford, 1963.
- 421 Albert, J. M., Ginet, G. P., and Gussenhoven, M. S.: CRRES observations of radiation belt protons,
422 1, Data overview and steady state radial diffusion, *J. Geophys. Res.*, **103**(A5), 9261–9273.
423 <https://doi.org/10.1029/97JA02869>, 1998.
- 424 Baumjohann, W.: The near-Earth plasma sheet: An AMPTE/IRM perspective, *Space Sci. Rev.*,
425 **64**(1–2), 141–163, <https://doi.org/10.1007/BF00819660>, 1993.
- 426 Blake, J. B., and Fennell, J. F.: Heavy ion measurements in the synchronous altitude region, *Planet.*
427 *Space Sci.*, **29**(11), 1205–1213, [https://doi.org/10.1016/0032.0633\(81\)90125-2](https://doi.org/10.1016/0032.0633(81)90125-2), 1981.
- 428 Blake, J. B., Fennell, J. F., Schulz, M., and Paulikas, G. A.: Geomagnetically trapped alpha
429 particles, 2, The inner zone, *J. Geophys. Res.*, **78**(25), 5498–5506,
430 <https://doi.org/10.1029/JA078i025p05498>, 1973.
- 431 Blanchard, R. C., and Hess, W. N.: Solar cycle changes in inner-zone protons, *J. Geophys. Res.*,
432 **69**(19), 3927–3938, <https://doi.org/10.1029/JZ069i019p03927>, 1964.
- 433 Chenette, D. L., Blake, J. B., and Fennell, J. F.: The charge state composition of 0.4–MeV helium
434 ions in the Earth’s outer radiation belts during quiet times, *J. Geophys. Res.*, **89**(A9), 7551–
435 7555, <https://doi.org/10.1029/JA089iA09p07551>, 1984.
- 436 Cheng, A. F., Krimigis, S. M., and Armstrong, T. P.: Near equality of ion phase space densities at
437 Earth, Jupiter, and Saturn, *J. Geophys. Res.*, **90**(A9), 526–530,
438 <http://doi.org/10.1029/JA090iA01p00526>, 1985.
- 439 Christon, S. P., Williams, D. J., Mitchell, D. G., Huang, C. Y., and Frank, L. A.: Spectral
440 characteristics of plasma sheet ion and electron populations during disturbed geomagnetic
441 conditions, *J. Geophys. Res.*, **96**(A1), 1–22, <https://doi.org/10.1029/90JA01633>, 1991.
- 442 Croley, D. R., Jr., Schulz, M., and Blake, J. B.: Radial diffusion of inner-zone protons:
443 Observations and variational analysis, *J. Geophys. Res.*, **81**(4), 585–594,
444 <https://doi.org/10.1029/JA081i004p00585>, 1976.
- 445 Dragt, A. J.: Solar cycle modulation of the radiation belt proton flux, *J. Geophys. Res.*, **76**(10),
446 2313–2344, <https://doi.org/10.1029/JA076i010p02313>, 1971.
- 447 Fennell, J. F., and Blake, J. B.: Geomagnetically trapped α -particles, *Magnetospheric Particles and*
448 *Fields*, edited by: McCormac, B. M., D. Reidel, Dordrecht, Holland, 149–156, 1976.
- 449 Filz, R. C.: Comparison of the low-altitude inner-zone 55–MeV trapped proton fluxes measured in
450 1965 and 1961–1962, *J. Geophys. Res.*, **72**(3), 959–963,
451 <https://doi.org/10.1029/JZ072i003p00959>, 1967.
- 452 Freden, S. C., Blake, J. B., and Paulikas, G. A.: Spatial variation of the inner zone trapped proton
453 spectrum, *J. Geophys. Res.*, **70**(13), 3113–3116, <https://doi.org/10.1029/JZ070i013p03113>,
454 1965.
- 455 Fritz, T. A., and Spjeldvik, W. N.: Observations of energetic radiation belt helium ions at the
456 geomagnetic equator during quiet conditions, *J. Geophys. Res.*, **83**(A6), 2579–2583,
457 <https://doi.org/10.1029/JA083iA06p02579>, 1978.

458 Fritz, T. A., and Spjeldvik, W. N.: Simultaneous quiet time observations of energetic radiation belt
459 protons and helium ions: The equatorial α/p ratio near 1 MeV, *J. Geophys. Res.*, **84**(A6),
460 2608–2618, <https://doi.org/10.1029/JA084iA06p02608>, 1979.

461 Fritz, T. A., and Spjeldvik, W. N.: Steady-state observations of geomagnetically trapped energetic
462 heavy ions and their implications for theory, *Planet. Space Sci.*, **29**(11), 1169–1193,
463 [https://doi.org/10.1016/0032-0633\(81\)90123-9](https://doi.org/10.1016/0032-0633(81)90123-9), 1981.

464 Ginzburg, V. L., and Syrovatskii, S. I.: *The Origin of Cosmic Rays*, Pergamon Press, Oxford,
465 1964.

466 Ginat, G. P., O'Brien, T. P., Huston, S. L., Johnston, W. R., Guild, T. B., Friedel, R., Lindstrom,
467 C. D., Roth, C. J., Whelan, P., Quinn, R. A., Madden, D., Morley, S., and Su, Yi-J.: AE9, AP9
468 and SPM: New models for specifying the trapped energetic particle and space plasma
469 environment, *Space Sci. Rev.*, **179**(1–4), 579–615, <https://doi.org/10.1007/s11214-013-9964-y>,
470 2013.

471 Goka, T., Matsumoto, H., and Takagi, S.: Empirical model based on the measurements of the
472 Japanese spacecrafts, *Radiation Measurements*, **30**(5), 617–624, [https://doi.org/10.1016/S1350-4487\(99\)00237-1](https://doi.org/10.1016/S1350-4487(99)00237-1), 1999.

474 Hess, W. N.: Discussion of paper by Pizzella, McIlwain, and Van Allen, 'Time variations of
475 intensity in the Earth's inner radiation zone, October 1959 through December 1960', *J.*
476 *Geophys. Res.*, **67**(12), 4886–4887, <https://doi.org/10.1029/JZ0670i012p04886>, 1962.

477 Hovestadt, D., Häusler, B., and Scholer, M.: Observation of energetic particles at very low
478 altitudes near the geomagnetic equator, *Phys. Rev. Lett.*, **28**(20), 1340–1343,
479 <https://doi.org/10.1103/PhysRevLett.28.1340>, 1972.

480 Hovestadt, D., Gloeckler, G., Fan, C. Y., Fisk, L. A., Ipavich, F.M., Klecker, B., O'Gallagher, J. J.,
481 and Scholer, M.: Evidence for solar wind origin of energetic heavy ions in the Earth's radiation
482 belt, *Geophys. Res. Lett.*, **5**(12), 1055–1057, <https://doi.org/10.1029/GL005i012p01055>, 1978.

483 Hovestadt, D., Klecker, B., Mitchell, E., Fennell, J. F., Gloeckler, G., and Fan, C. Y.: Spatial
484 distribution of $Z \geq 2$ ions in the outer radiation belt during quiet conditions, *Adv. Space Res.*,
485 **1**(1), 305–308, [https://doi.org/10.1016/0273-1177\(81\)90125-3](https://doi.org/10.1016/0273-1177(81)90125-3), 1981.

486 Huston, S., Kuck, G., and Pfitzer, K.: Low-altitude trapped radiation model using TIROS/NOAA
487 data, *Radiation Belts: Models and Standards*, edited by: Lemaire, J. F., Heynderickx, D., and
488 Baker, D. N., AGU, Washington, D. C., 119–122, <https://doi.org/10.1029/GM097/p0119>, 1996.

489 Ilyin, B. D., Kuznetsov, S. N., Panasyuk, M. I., and Sosnovets, E.N.: Non-adiabatic effects and
490 boundary of the trapped protons in the Earth's radiation belts, *Bulletin of the Russian Academy*
491 *of Sciences: Physics*, **48**(11), 2200–2203, 1984.

492 Ipavich, F. M., Galvin, A. B., Gloeckler, G., Scholer, M., and Hovestadt D.: A statistical survey of
493 ions observed upstream of the Earth's bow shock: Energy spectra, composition, and spatial
494 variation, *J. Geophys. Res.*, **86**(A6), 4337–4342, <https://doi.org/10.1029/JA086iA06p4337>,
495 1981a.

496 Ipavich, F. M., Scholer, M., and Gloeckler, G.: Temporal development of composition, spectra,
497 and anisotropies during upstream particle events, *J. Geophys. Res.*, **86**(A13), 11153–11160,
498 <https://doi.org/10.1029/JA086iA13p11153>, 1981b.

499 Kollmann, P., Roussos, E., Paranicas, C., Krupp, N., Jackman, C. M., Kirsch, E., and Glassmeier,
500 K.-H.: Energetic particle phase space densities at Saturn: Cassini observations and
501 interpretations, *J. Geophys. Res. Space Phys.*, **116**(A5), A05222,
502 <https://doi.org/10.1029/2010JA016221>, 2011.

503 Kovtyukh, A. S.: Geocorona of hot plasma, *Cosmic Res.*, **39**(6), 527–558,
504 <https://doi.org/10.1023/A:1013074126604>, 2001.

505 Kovtyukh, A. S.: Radial dependence of ionization losses of protons of the Earth's radiation belts,
506 *Ann. Geophys.*, **34**(1), 17–28, <https://doi.org/10.5194/angeo-34-17-2016>, 2016a.

507 Kovtyukh, A. S.: Deduction of the rates of radial diffusion of protons from the structure of the
508 Earth's radiation belts, *Ann. Geophys.*, **34**(11), 1085–1098. [https://doi.org/10.5194/angeo-34-](https://doi.org/10.5194/angeo-34-1085-2016)
509 [1085-2016](https://doi.org/10.5194/angeo-34-1085-2016), 2016b.

510 Kovtyukh, A. S.: Ion Composition of the Earth's Radiation Belts in the Range from 100 keV to
511 100 MeV/nucleon: Fifty Years of Research, *Space Sci. Rev.*, **214**(8), 124:1–124:30,
512 <https://doi.org/10.1007/s11214-018-0560-z>, 2018.

513 Krimigis, S. M.: Alpha particles trapped in the Earth's magnetic field, *Particles and Fields in the*
514 *Magnetosphere*, edited by: McCormac, B. M., D. Reidel, Dordrecht, Holland, 364–379, 1970.

515 Krimigis, S. M., Carbary, J. F., Keath, E. P., Bostrom, C. O., Axford, W. I., Gloeckler, G.,
516 Lanzerotti, L. J., and Armstrong, T. P.: Characteristics of hot plasma in the Jovian
517 magnetosphere: Results from the Voyager spacecraft, *J. Geophys. Res.*, **86**(A10), 8227–8257.
518 <http://doi.org/10.1029/JA086iA10p08227>, 1981.

519 Kuznetsov, N. V., Nikolaeva, N. I., and Panasyuk, M. I.: Variation of the trapped proton flux in the
520 inner radiation belt of the Earth as a function of solar activity, *Cosmic Res.*, **48**(1), 80–85,
521 <https://doi.org/10.1134/S0010952510010065>, 2010.

522 Lui, A. T. Y., and Krimigis, S. M.: Several features of the earthward and tailward streaming of
523 energetic protons (0.29–0.5 MeV) in the Earth's plasma sheet, *J. Geophys. Res.*, **86**(A13),
524 11173–11188, <https://doi.org/10.1029/JA086iA13p11173>, 1981.

525 Lutsenko, V. N., and Nikolaeva, N. S.: Relative content and the range of alpha particles in the
526 inner radiation belt of the Earth by measurements on satellite Prognoz-5, *Cosmic Res.*, **16**(3),
527 459–462, 1978.

528 Mazur, J. E., Mason, G. M., Blake, J. B., Klecker, B., Leske, R. A., Looper, M. D., and Mewaldt,
529 R. A.: Anomalous cosmic ray argon and other rare elements at 1–4 MeV/nucleon trapped within
530 the Earth's magnetosphere, *J. Geophys. Res.*, **105**(A9), 21015–21023,
531 <https://doi.org/10.1029/1999JA000272>, 2000.

532 McIlwain, C. E.: Coordinate for mapping the distribution of magnetically trapped particles, *J.*
533 *Geophys. Res.*, **66**(11), 3681–3691, <https://doi.org/10.1029/JZ066i011p03681>, 1961.

534 Milovanov, A. V., Zelenyi, L. M., and Zimbardo, G.: Fractal structures and power low spectra in
535 the distant Earth's magnetotail, *J. Geophys. Res. Space Phys.*, **101**(A9), 19903–19910,
536 <https://doi.org/10.1029/96JA01562>, 1996.

537 Nakano, G., and Heckman, H.: Evidence for solar-cycle changes in the inner-belt protons, *Phys.*
538 *Rev. Lett.*, **20**(15), 806–809, <https://doi.org/10.1103/PhysRevLett.20.806>, 1968.

539 Northrop, T. G.: *The Adiabatic Motion of Charged Particles*, Wiley-Interscience, NY, USA, 1963.

540 Panasyuk, M. I., and Sosnovets, E. N.: Differential energy spectrum of low-energy protons in the
541 inner region of the radiation belt, *Cosmic Res.*, **11**(3), 436–440, 1973.

542 Panasyuk, M. I., Reizman, S. Ya., Sosnovets, E. N., and Filatov, V. N.: Experimental results of
543 protons and α -particles measurements with energy more 1 MeV/nucleon in the radiation belts,
544 *Cosmic Res.*, **15**(6), 887–894, 1977.

545 Pizzella, G., McIlwain, C. E., and Van Allen, J. A.: Time variations of intensity in the Earth's
546 inner radiation zone, October 1959 through December 1960, *J. Geophys. Res.*, **67**(4), 1235–
547 1253, <https://doi.org/10.1029/JZ067i004p01235>, 1962.

548 Pizzella, G., and Randall, B. A.: Differential energy spectrum of geomagnetically trapped protons
549 with the Injun 5 satellite, *J. Geophys. Res.*, **76**(10), 2306–2312,
550 <https://doi.org/10.1029/JA076i010p02306>, 1971.

551 Qin, M., Zhang, X., Ni, B., Song, H., Zou, H., and Sun, Y.: Solar cycle variations of trapped
552 proton flux in the inner radiation belt, *J. Geophys. Res. Space Phys.*, **119**(12), 9658–9669,
553 <https://doi.org/10.1002/2014JA020300>, 2014.

554 Sarris, E. T., Krimigis, S. M., Lui, A. T. Y., Ackerson, K. L., Frank, L. A., and Williams, D. J.:
555 Relationship between energetic particles and plasmas in the distant plasma sheet, *Geophys. Res.*
556 *Lett.*, **8**(4), 349–352, <https://doi.org/10.1029/GL008i004p0349>, 1981.

557 Schulz, M., and Lanzerotti, L. J.: Particle Diffusion in the Radiation Belts, Springer, NY, USA,
558 1974.

559 Selesnick, R. S., Looper, M. D., and Mewaldt, R. A.: A theoretical model of the inner proton
560 radiation belt, *Space Weather*, **5**(4), S04003, <https://doi.org/10.1029/2006SW000275>, 2007.

561 Selesnick, R. S., Hudson, M. K., and Kress, B. T.: Injection and loss of inner radiation belt protons
562 during solar proton events and magnetic storms, *J. Geophys. Res. Space Phys.*, **115**(A8),
563 A08211, <https://doi.org/10.1029/2010JA015247>, 2010.

564 Selesnick, R. S., Hudson, M. K., and Kress B. T.: Direct observation of the CRAND proton
565 radiation belt source, *J. Geophys. Res. Space Phys.*, **118**(12), 7532–7537,
566 <https://doi.org/10.1002/2013JA019338>, 2013.

567 Selesnick, R. S., Baker, D. N., Jaynes, A. N., Li, X., Kanekal, S. G., Hudson, M. K., and Kress, B.
568 T.: Observations of the inner radiation belt: CRAND and trapped solar protons, *J. Geophys.
569 Res. Space Phys.*, **119**(8), 6541–6552, <https://doi.org/10.1002/2014JA020188>, 2014.

570 Selesnick, R. S., Baker, D. N., Kanekal, S. G., Hoxie, V. C., and Li, X.: Modeling the proton
571 radiation belt with Van Allen Probes Relativistic Electron-Proton Telescope data, *J. Geophys.
572 Res. Space Phys.*, **123**(1), 685–697, <https://doi.org/10.1002/2017JA024661>, 2018.

573 Selesnick, R. S., and Albert, J. M.: Variability of the proton radiation belt, *J. Geophys. Res. Space
574 Phys.*, **124**(7), 5516–5527, <https://doi.org/10.1029/2019JA026754>, 2019.

575 Spjeldvik, W. N.: Expected charge states of energetic ions in the magnetosphere, *Space Sci. Rev.*,
576 **23**(3), 499–538, <https://doi.org/10.1007/BF00172252>, 1979.

577 Spjeldvik, W. N., and Fritz, T. A.: Quiet time observations of equatorially trapped
578 megaelectronvolt radiation belt ions with nuclear charge $Z \geq 4$, *J. Geophys. Res.*, **83**(A9), 4401–
579 4405, <https://doi.org/10.1029/JA083iA09p04401>, 1978.

580 Spjeldvik, W. N., and Fritz, T. A.: Observations of energetic helium ions in the Earth's radiation
581 belts during a sequence of geomagnetic storms, *J. Geophys. Res.*, **86**(A4), 2317–2328,
582 <https://doi.org/10.1029/JA086iA04p02317>, 1981.

583 Stevens, J. R., Martina, E. F., and White, R. S.: Proton energy distributions from 0.060 to 3.3 MeV
584 at 6.6 Earth radii, *J. Geophys. Res.*, **75**(28), 5373–5385,
585 <https://doi.org/10.1029/JA075i028p05373>, 1970.

586 Usoskin, I. G., Alanko-Huotari, K., Kovaltsov, G. A., and Mursula, K.: Heliospheric modulation of
587 cosmic rays: Monthly reconstruction for 1951–2004, *J. Geophys. Res.*, **110**(A12), A12108,
588 <https://doi.org/10.1029/2005JA011250>, 2005.

589 Vacaresse, A., Boscher, D., Bourdarie, S., Blanc, M., and Sauvaud, J. A.: Modeling the high-
590 energy proton belt, *J. Geophys. Res. Space Phys.*, **104**(A12), 28601–28613,
591 <https://doi.org/10.1029/1999JA900411>, 1999.

592 Venkatesan, D., and Krimigis, S. M.: Observations of low-energy (0.3– to 1.8-MeV) differential
593 spectrums of trapped protons, *J. Geophys. Res.*, **76**(31), 7618–7631,
594 <https://doi.org/10.1029/JA076i031p07618>, 1971.

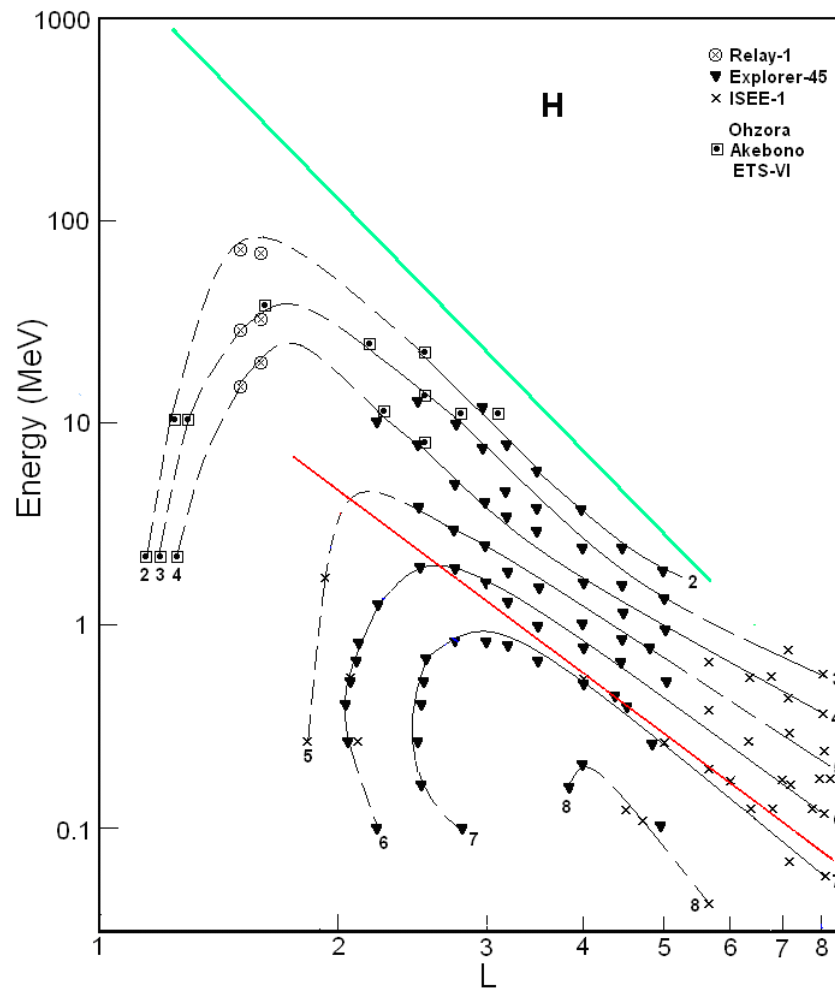
595 Vernov, S. N.: The Earth's radiation belts. In G. Bozóki, E. Gombosi, A. Sebastyén, A. Somogyi
596 (Eds.), *Proc. 11th ICRC, Budapest*, 85–162, 1969.

597 Westphalen, H., and Spjeldvik, W.N.: On the energy dependence of the radial diffusion coefficient
598 and spectra of inner radiation belt particles: Analytic solution and comparison with numerical
599 results, *J. Geophys. Res.*, **87**(A10), 8321–8326, <https://doi.org/10.1029/2000JA087iA10p08321>,
600 1982.

601 Wilken, B., Baker, D. N., Highbie, P. R., Fritz, T. A., Olson, W. P., and Pfitzer, K. A.:
602 Magnetospheric configuration and energetic particle effects associated with a SSC: A case study
603 of the CDAW 6 event on March 22, 1979, *J. Geophys. Res.*, **91**(A2), 1459–1473,
604 <https://doi.org/10.1029/JA091iA02p01459>, 1986.

605 Williams, D. J.: Phase space variations of near equatorially mirroring ring current ions, *J. Geophys.
606 Res.*, **86**(A1), 189–194, <https://doi.org/10.1029/JA086iA01p00189>, 1981.

607 Williams, D. J., and Frank, L. A.: Intense low-energy ion populations at low equatorial altitude, *J.*



609

610

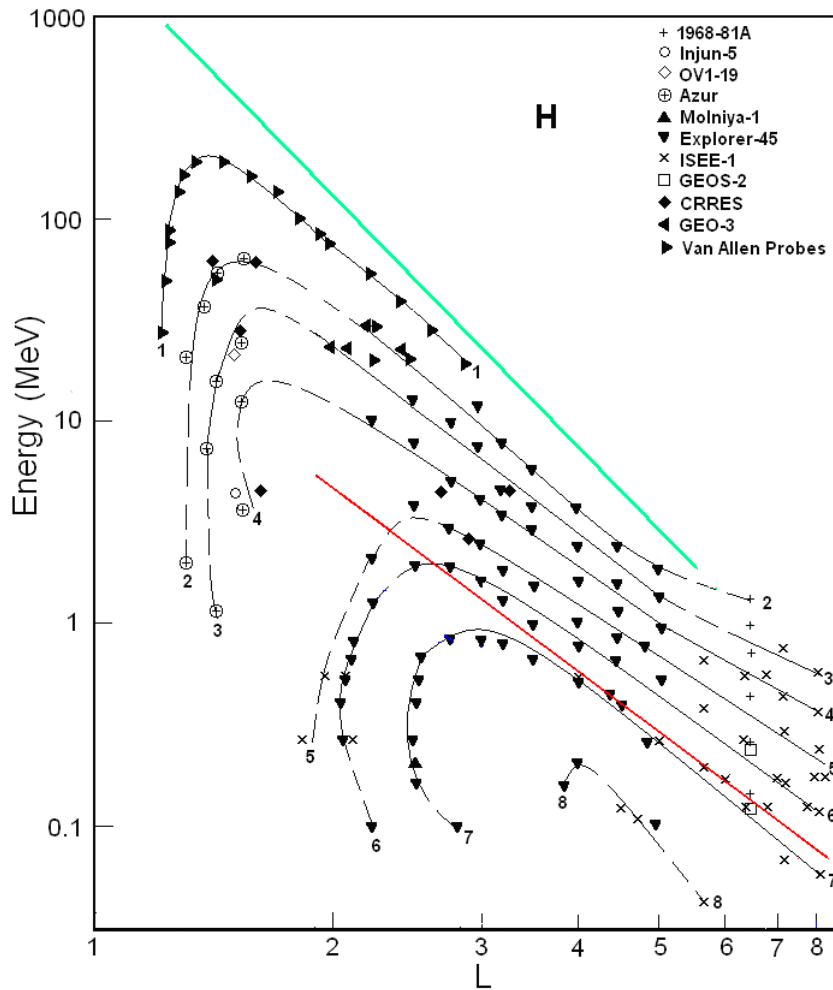
611

612

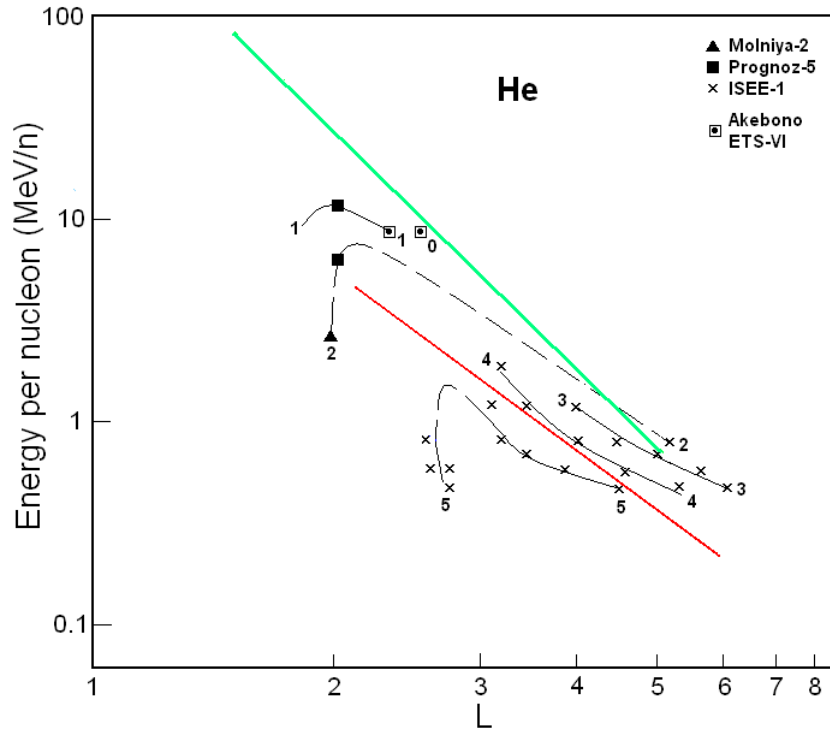
613

614

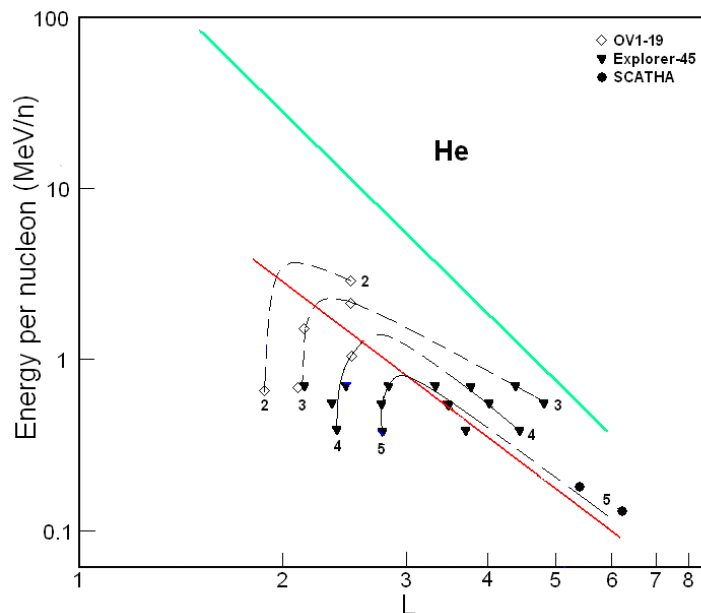
Figure 1. Proton fluxes in the ERB near minima of the solar activity. The numbers on the curves refer to the values of the decimal logarithms of J , which is given in units of $(\text{cm}^2 \text{ s ster MeV})^{-1}$, is the differential fluxes of protons with $\alpha_0 \approx 90^\circ$ (near the plane of the geomagnetic equator). Data of satellites are associated with different symbols. The red line corresponds to the lower boundary of the power-law tail of the proton spectra; while green line corresponds to the maximum energy of protons trapped in the ERB (Ilyin et al., 1984).



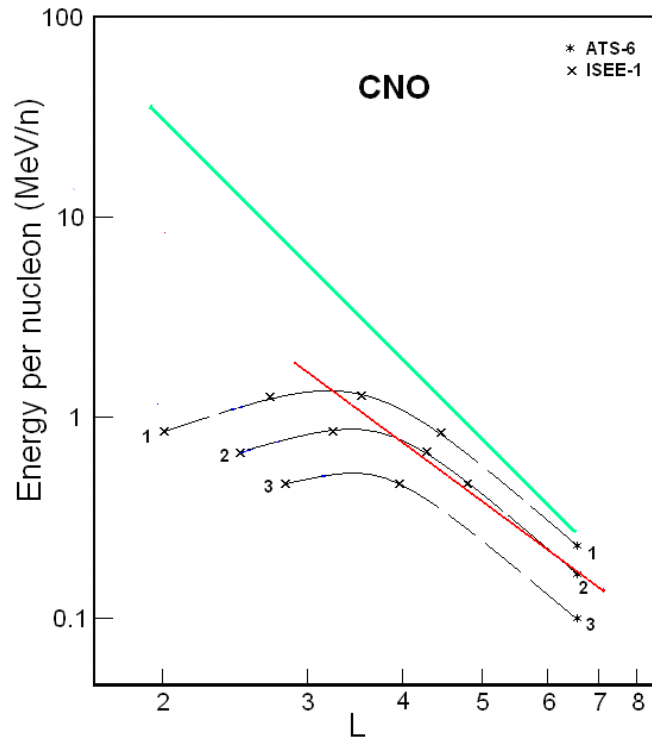
615
 616 **Figure 2.** Proton fluxes in the ERB near maxima of the solar activity. The numbers on the curves refer to the values of
 617 the decimal logarithms of J , which is given in units of $(\text{cm}^2 \text{ s ster MeV})^{-1}$, is the differential fluxes of protons with $\alpha_0 \approx$
 618 90° (near the plane of the geomagnetic equator). Data of satellites are associated with different symbols. The red line
 619 corresponds to the lower boundary of the power-law tail of the proton spectra; while green line corresponds to the
 620 maximum energy of protons trapped in the ERB (Ilyin et al., 1984).



621
 622 **Figure 3.** Helium ion fluxes in the ERB near minima of the solar activity. The numbers on the curves refer to the
 623 values of the decimal logarithms of J , which is given in units of $(\text{cm}^2 \text{ s ster MeV/n})^{-1}$, is the differential fluxes of
 624 helium ions with $\alpha_0 \approx 90^\circ$ (near the plane of the geomagnetic equator). Data of satellites are associated with different
 625 symbols. The red line corresponds to the lower boundary of the power-law tail of the helium spectra; while green line
 626 corresponds to the maximum energy of these ions trapped in the ERB (Ilyin et al., 1984).

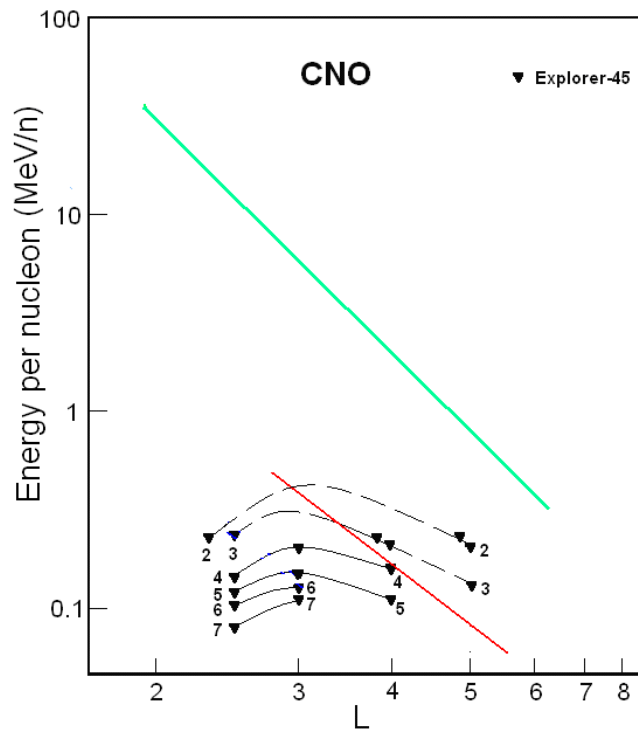


627
 628 **Figure 4.** Helium ion fluxes in the ERB near maxima of the solar activity. The numbers on the curves refer to the
 629 value of the decimal logarithms of J which is given in units of $(\text{cm}^2 \text{ s ster MeV/n})^{-1}$, is the differential fluxes of ions
 630 with $\alpha_0 \approx 90^\circ$ (near the plane of the geomagnetic equator). Data of satellites are associated with different symbols. The
 631 red line corresponds to the lower boundary of the power-law tail of the helium spectra; while green line corresponds to
 632 the maximum energy of these ions trapped in the ERB (Ilyin et al., 1984).



633
634
635
636
637
638

Figure 5. CNO ion fluxes in the ERB near minima of the solar activity. The numbers on the curves refer to the values of the decimal logarithms of J , which is given in units of $(\text{cm}^2 \text{ s ster MeV/n})^{-1}$, is the differential fluxes of ions with $\alpha_0 \approx 90^\circ$ (near the plane of the geomagnetic equator). Data of satellites are associated with different symbols. The red line corresponds to the lower boundary of the power-law tail of the CNO ion spectra; while green line corresponds to the maximum energy of these ions trapped in the ERB (Ilyin et al., 1984).



639
640
641
642
643
644

Figure 6. CNO ion fluxes in the ERB near the maximum of the solar activity. The numbers on the curves refer to the values of the decimal logarithms of J , which is given in units of $(\text{cm}^2 \text{ s ster MeV/n})^{-1}$, is the differential fluxes of ions with $\alpha_0 \approx 90^\circ$ (near the plane of the geomagnetic equator). Data of satellites are associated with different symbols. The red line corresponds to the lower boundary of the power-law tail of the CNO ion spectra; while green line corresponds to the maximum energy of these ions trapped in the ERB (Ilyin et al., 1984).